

# Journal of Biomedical Optics

SPIEDigitalLibrary.org/jbo

## **Differential optical spectropolarimetric imaging system assisted by liquid crystal devices for skin imaging**

Ofir Aharon  
Ibrahim Abdulhalim  
Ofer Arnon  
Lior Rosenberg  
Victor Dyomin  
Eldad Silberstein

# Differential optical spectropolarimetric imaging system assisted by liquid crystal devices for skin imaging

Ofir Aharon,<sup>a</sup> Ibrahim Abdulhalim,<sup>a</sup> Ofer Arnon,<sup>b</sup> Lior Rosenberg,<sup>b,c</sup> Victor Dyomin,<sup>d</sup> and Eldad Silberstein<sup>b</sup>

<sup>a</sup>Ben Gurion University of the Negev, Department of Electro-Optic Engineering, Beer Sheva 84105, Israel

<sup>b</sup>Soroka Hospital, Department of Plastic and Reconstructive Surgery and Burn Unit, Beer Sheva, 84105 Israel

<sup>c</sup>Ben Gurion University of the Negev, University Medical Center, Beer Sheva, 84105, Israel

<sup>d</sup>Soroka Hospital, Pathology Institute, Beer Sheva, 84105 Israel

**Abstract.** Skin cancer diagnosis depends not only on histopathological examination but also on visual inspection before and after the excision of suspected lesion. Neoplasm is accompanied with changes in birefringence of collagen, pleomorphicity, and hyperchromatic state of epithelial nuclei. These phenomena can be measured by spectral and polarization changes of light backscattered by the examined tissue. A new differential spectropolarimetric system is proposed using liquid crystal devices, one as a tunable filter and the other as a polarization rotator, both operating at wide spectral ranges from the visible to the near-infrared. Since collagen's fibrils texture orientation depends on its location in the skin and since it is not well organized, our system scans the bipolarization states by continuously rotating the linearly polarized light incident on a skin lesion, and collecting differential contrasts between sequenced images when simultaneously averaging the statistical readout of a video camera. This noninvasive method emphasizes areas on skin where the neoplasm, or tumor, minimizes the statistical polarization change of the scattered light from the lesion. The module can be considered as an assistant tool for epiluminescence microscopy. Images of skin tumors were captured *in vivo* before the patients having their surgery and compared to histopathological results. © 2011 Society of Photo-Optical Instrumentation Engineers (SPIE). [DOI: 10.1117/1.3609003]

Keywords: skin imaging; skin cancer; spectral imaging; polarimetric imaging.

Paper 11089R received Mar. 2, 2011; revised manuscript received Jun. 9, 2011; accepted for publication Jun. 17, 2011; published online Aug. 1, 2011.

## 1 Introduction

According to the American Cancer Society<sup>1</sup> the most serious form of skin cancer is cutaneous malignant melanoma (CMM), with an incidence of about 67,720 in the U.S. annually, with about 8650 out of the 11,590 skin cancer deaths. CMM is curable at its earliest stages, but it is resistant to any current medical treatment once it metastasizes. Early detection of the CMM disease is therefore very important. CMM often starts as small, mole-like growths that increase in size and may change color. A common method used by physicians to diagnose skin cancer is the ABCD rule,<sup>2</sup> However, performance of dermatoscopic examination is still strongly influenced by ones, experience and ends with a high rate of false-positive skin cancer diagnosis. CMM may start as an innocent pigmented lesion that is hard to diagnose and ends with fatal metastasis. Therefore, for the last 30 years researchers put a lot of endeavors to find a noninvasive, simpler, and time-efficient method for an objective way to diagnose skin cancer. Skin lesion can be investigated at the microscopic and the macroscopic scales in two main paths, 1 the changes in color and 2 the changes in tissue structure, as the result in different size of the cell nuclei and denaturation of the collagen. Collagen denaturation affects the birefringence due to deformation of regular molecular binding structure.<sup>3-5</sup> It is known that the majority of epithelial cancers are preceded by precancerous changes that affect both epithelium surface and deeper stroma. Biochemical and morphological changes asso-

ciated with precancer perturb several parameters such as tissue absorption, scattering, and fluorescence properties. Thus, polarized optical spectroscopy may probe precancerous changes. There is vast interest nowadays in the macroscopic scale diagnosis, which mainly uses the fact that precancer is accompanied by local metabolic and architectural changes at the cellular and sub-cellular level. Before they become invasive, at stages known as dysplasia or carcinoma *in situ*, early cancer cells alter the epithelial cells architecture.<sup>6,7</sup> For sources in the tissue that cause polarization change in backscattered light one can summarize that primary scatterers are: the collagen fiber network of extracellular matrix,<sup>8</sup> mitochondria, and other intracellular substructures. Changes in the polarization state of backscattered light from a turbid medium are well known. Seeking this phenomena in skin tissue was initiated in 1988 by Philp et al.<sup>9</sup> followed by Anderson.<sup>10</sup> In 2003, Anderson et al. used their method for skin lesion boundary detection in Mohs micrographic surgery (MMS),<sup>11</sup> an enhanced view of vasculature and pigmented lesions was obtained. In 2004, Boulesteix et al.<sup>12</sup> extracted the degree of polarization (DOP) for stained hepatic biopsy from Mueller matrices at visible and near-infrared spectral regions. Anomalous structure of collagen was emphasized at different wavelengths. In the same year Ramella et al.<sup>13</sup> simplified the readout of two polarizations (parallel and crossed polarizations with respect to the light source polarization) from tissue by using two CCD cameras, and calculated the normalized contrast between them simultaneously ( $S_1$  parameter of Stokes vector). Weber et al.<sup>14</sup> manipulated the cross and parallel polarizations separately so a tiny vein in the eye could be recognized. In 2005,

Address all correspondence to: Ofir Aharon, Ben Gurion University, Electro-Optic Engineering, P. O. Box 653, Beer Sheva, 84105 Israel; Tel: 97208647903; E-mail: ofir.academic@gmail.com, www.dosiscan.com.

1083-3668/2011/16(8)/086008/12/\$25.00 © 2011 SPIE

Ramella et al.<sup>15</sup> described a better way to illuminate tissue by skewed illumination for backscattered imaging. This allowed them to eliminate the glare with no need for oil or water as a matching refractive index.

The endless forms and thicknesses of a damaged tissue can come either as a nevus, neoplasm, or even a burned skin, to elude upon the legitimacy to seek an arbitrary way of scanning skin lesion. Our main goal is to develop a technology that will enable to diagnose seemingly “innocent” pigmented lesions that can lead eventually to metastasis. Our hypothesis is that macroscopic changes due to dysplasm will generate differences in the backscattered light which may help for precursor cancer diagnosis. Our differential optical spectropolarimetric imaging (DOSI) system utilizes these characteristics to distinguish intradermal structural changes in precancerous tissue by continuous polarimetric control, using two wavelengths in this case study of 520 and 700 nm. The incident light on the lesion is linearly polarized and continuously rotated. At the same time, a digital camera captures a sequence of pictures which will be sent to a differential image processing algorithm which we proposed. The wavelength selection and the polarization control were performed by our new liquid crystal devices (LCDs) managed by an in-house LABVIEW program. Post-processing of captured images by DOSI presents a way to distinguish between different patterns of benign lesions and dysplasm that might lead to CMM.

## 2 Materials and Methods

### 2.1 Differential Spectropolarimetric Imaging System Using Liquid Crystal Devices

The DOSI system comprises a halogen light source with collimation and imaging optics, using liquid crystal tunable filter (LCTF) with linearly polarized output and a wavelength independent liquid crystal (LC) polarization rotator (WILCPR). The LCTF<sup>16</sup> and the WILCPR<sup>17,18</sup> were designed and fabricated in our clean room, especially for the DOSI system. The LCTF and the WILCPR are both controlled by sinusoidal voltages at 1 kHz to generate color and continuous rotation of the linearly polarized light illuminating the investigated lesion. A CCD camera with fixed polarizer captures a sequence of pictures (as uncompressed movie). After image capture, a MATLAB<sup>®</sup> program calculates the contrast between two adjacent pictures and averages a chosen section of picture series.

The DOSI system diagram is shown in Fig. 1, (A) is halogen light source with lens to collimate light to LCTF (B), light emerges from LCTF linearly polarized, entering WILCPR (C) and impinges on glass window (D), touching the examined skin lesion. Backreflected light emitted toward fixed polarizer (E) objective (F) and CCD camera (G). A computer (H) controls DOSI scan with function generator NI6715-PCMCIA card (analog output voltage of 8 channels).<sup>19</sup> Polarized light is obliquely incident while the read light is symmetric around the normal to the surface being inspected,<sup>20</sup> and the configuration in this work uses LC devices with new algorithms that will be explained later on.

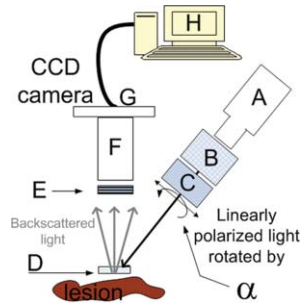


**Fig. 1** DOSI imager using LCDs. (A) is halogen light source with lens to collimate light to LCTF (B), light emerges from LCTF linearly polarized, entering WILCPR (C) and impinges on the glass window (D), touching the examined skin lesion. Backreflected light emitted toward fixed polarizer (E) objective (F) and CCD camera (G). A computer (H) controls DOSI scan with function generator NI6715-PCMCIA card.

In Fig. 1 the LCTF (B) and WILCPR (C) are controlled by the FG. The scanning performed by first choosing the wavelength with the LCTF and then rotating the linearly polarized light using the WILCPR. The incident light (on the lesion), linearly polarized and rotated three cycles. The angle velocity was 1 rotation for 2 s, 60 frames for 1 rotation. The scan lingered for 6 s, thus generating 180 pictures. For each angle of rotation  $\alpha$ , the backscattered light is captured as frames on the 8-bit CCD camera with resolution of  $640 \times 480$ , IEEE type. In front of the camera we located a fixed wire-grid linear polarizer. The advantage of using a wire-grid polarizer over the polaroid polarizer is that it covers the visible (VIS) and the near-infrared (NIR) spectral ranges. The computer (H) in our case is a laptop with National instruments function generator, type: NI6715-PCMCIA card (analog output voltage of 8 channels) and a FireWire connection to a CCD camera. Figure 2 shows the whole pack — the DOSI system and the laptop, the whole system can be carried in one laptop bag. To control the image capture process we developed a LABVIEW program as shown in Fig. 3. This interface has two purposes: the first is for the calibration of LCTF and WILCPR, when necessary, and the second is for capturing a sequence of images *in vivo*.

LCTF and WILCPR retarders were built using glass substrates of area  $15 \text{ mm} \times 17 \text{ mm}$  and thickness of 2 mm. The two pieces of flat glass coated with transparent electrically conducting electrodes made of indium tin oxide were cleaned and spin coated with Rolic photoalignment polymer linearly photopolymerisation. A spinner was set to 4000 rpm for 60 s to form  $\sim 50 \text{ nm}$  of uniform polymer thickness. Then, polymer was baked in a vacuum oven at a temperature of  $90^\circ\text{C}$  for 30 min

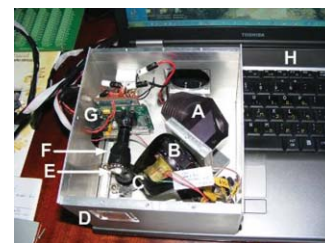


**Fig. 2** DOSI system including one laptop that can be portable in a school bag. Under operation the upper sealing is closed to eliminate background light.

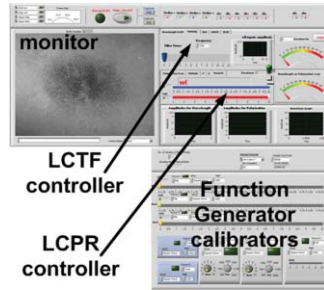


**Fig. 3** LABVIEW program interface for calibration of liquid crystal devices (LCTF, WILCPR) and capturing a sequence of images while rotating the polarization of light impinging on the tissue.

and then at a temperature of 250°C for 1 h. Next, the two polymer coated substrates were irradiated by a collimated linearly polarized UV light at normal incidence for photoalignment. After UV irradiation for photoalignment, glass spacers mixed with UV-glue Norland 68 were applied near the edges of the glass substrates. Assembling the two glass plates was then achieved with a specially designed mechanical jig to obtain a uniform gap by observing the interference colors reflected from the empty cell with a green light. The cell then was filled with the nematic LC 4-pentyl-4'-cyanobiphenyl (E44) purchased from Merck, in vacuum, at a temperature above the clearing temperature (101°C in our case), and then cooled slowly to room temperature. The cell was sealed with UV-glue Norland 68 and metal wires connected to electrodes using sliver paste and epoxy glue. Characterization of the LC thickness was done by spectral measurement of the retardation between crossed polarizers and using fitting of measured output spectrum with theoretical spectrum. Our polarizers are limited to the wavelength regime between 450 and 850 nm. Retarders were aligned in a setup which enabled us to rotate them freely and modify their voltage. Output transmission spectrum was read by a spectrometer manufactured by StellarNet Inc-EPP2000. Each glass surface attenuates 4% (transmittance 0.96<sup>2</sup> for each cell) and the polarizer attenuates 30% (transmits 0.7), thus the total transmission was 17%. However for bioimaging applications where CCD cameras are very sensitive it is not a problem to compensate with a stronger light source. It is also possible to use higher throughput polarizers such as those made of metal wire grids with transmission above 90%, bringing the filter output to nearly 50%. All retarders are controlled by our LABVIEW program code using National Instrument PCICIA Card NI6715 with eight programmable output voltage channels that we synchronized with the LABVIEW video code of the IEEE camera.

## 2.2 Functionality of the Liquid Crystal Devices

LCs are characterized by a large optical anisotropy, large electrooptic effect, fast tunability, and ease of fabrication.<sup>21,22</sup> These facts make them excellent candidates for tunable filtering and polarization control for biomedical optical applications.<sup>23</sup> LCTF is a birefringence filter that utilizes retardation between the ordinary and extraordinary light rays passing through the LC, creating constructive and destructive interferences, allowing a transmission of narrow spectral bands. By combining several electronically tunable LC retarders in series, a high spectral resolution can be achieved. LCTFs have the advantages of minia-

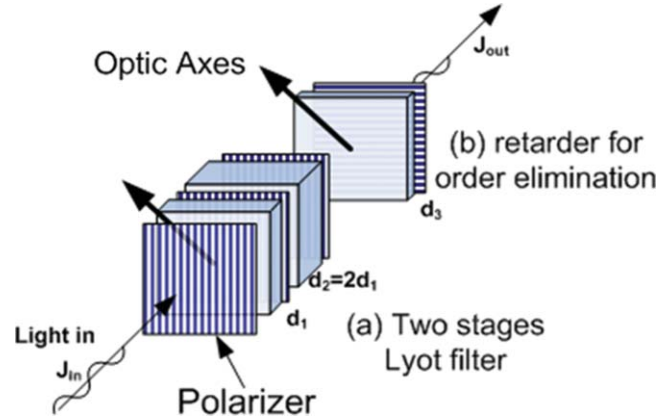


**Fig. 4** Lyot eliminated order filter (LEO filter) comprised from two parts (a) liquid crystal Lyot filter composed of two LCTRs,  $d$  is the first retarder thickness, (b) an additional LCTR between crossed polarizers to improve the free spectral range.

turization of the designed system, as well as tuning the center wavelength with no physical movements with capability of rapid wavelength selection in microsecond to tens of milliseconds tuning speeds.

Our LCTF is comprised of three retarders, two in Lyot–Öhman composition,<sup>24–26</sup> and an additional retarder between crossed polarizers, see Fig. 4(b). We named this filter as Lyot elimination order, or LEO filter, due to the additional retarder eliminating one of orders of Lyot filter, and by that extending its free spectral range. This latter property is needed in our imaging process to avoid disturbance of unwanted spectral order (named also mode). Transmission ( $T_{out}$ ) of the LEO filter was calculated by Jones matrices,<sup>27</sup> shown in Eq. (1). Equation (2) defines the retardation  $\delta_i$  for the LCTF retarders and the filter transfer function is given in Eq. (1):

$$T_{out} = \left[ \cos\left(\frac{\delta_1}{2}\right) \cos\left(\frac{\delta_2}{2}\right) \right] \sin\left(\frac{\delta_3}{2}\right)^2, \quad (1)$$

$$\delta_i = \frac{2\pi}{\lambda} \int_0^{d_i} \{n_e[\theta_i(z, V_i)] - n_o\} dz \quad (2)$$

$$i = 1, 2, 3, 4, 5,$$

where  $\lambda$  is the wavelength in vacuum,  $z$  is the coordinate normal to the LC retarders facets,  $n_e$  is the extraordinary index of refraction which depends on the LC molecules tilt angle  $\theta$ , and  $n_o$  is the ordinary index of refraction. The tilt angle profile  $\theta(z, V)$  depends on the external voltage and on the surface anchoring conditions. In reality, the angle of the LC molecules is governed by a nonlinear differential equation<sup>28</sup> which results in a larger angle in the middle of the LC layer compared to its boundaries. Very useful approximate analytic solutions have been proposed recently for the liquid crystal profile under voltage.<sup>29</sup>  $V_i$  is the applied voltages on each retarder,  $i = 1, 2, 3$  for the LCTF and  $i = 4, 5$  for the WILCPR. Retarder thicknesses of the LEO filter are  $d_1 = 8899$  nm,  $d_2 = 16043$  nm [Fig. 4(a)], and  $d_3 = 2600$  nm [Fig. 4(b)], while the deviation from  $d_2 = 2d_1$  (as should be in Lyot filter), was corrected by tuning the voltage on the first retarder  $d_1$ . The spectral dynamic range covering VIS and NIR (400 to 900 nm) is shown in Fig. 5 (normalized intensity).

Although the LCTF is capable of tuning over a wide spectral range, we concentrate in this study mainly on results obtained

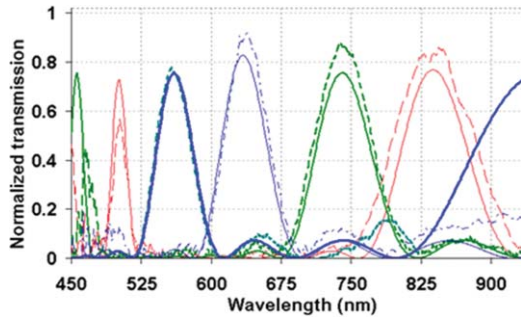


**Fig. 5** Normalized transmission of the LEO filter (dashed lines) and the theoretical calculation (solid lines) for the 2nd order peak of the Lyot filter at 838, 740, 634, and 560 nm when the sets of voltages for the first and second Lyot’s retarders, as well as for the additional eliminator retarder, were:  $\{V_1, V_2, V_3\} = \{2.23 \text{ V}, 2 \text{ V}, 2.16 \text{ V}\}$ ,  $\{2.492 \text{ V}, 2.28 \text{ V}, 2.455 \text{ V}\}$ ,  $\{2.785 \text{ V}, 2.61 \text{ V}, 2.79 \text{ V}\}$ ,  $\{3.0625 \text{ V}, 2.915 \text{ V}, 3.105 \text{ V}\}$ , correspondingly.

with two wavelengths: 520 and 700 nm based on two properties that can be inferred from the work of Zhang et al.<sup>30</sup> (Figs. 5–7): i. the large difference between the remittance at 520 and 700 nm and ii. the spectral dependence around each of these wavelengths is nearly flat. Zhang et al. performed their research on an Asian male with dark red skin and a Caucasian male with light-pink skin. As a rule of thumb, these types of skin are typical among all kinds of skin and surely suitable for a spectral decision of our preferable wavelengths. A similar phenomenon in darker skin was reported by Anderson et al. (Fig. 5).<sup>4</sup> Another reason for choosing these wavelengths, 520 and 700 nm, is the fact that penetration depths of 0.1 and 0.25 mm, respectively, as was shown by Anderson et al.<sup>11</sup> allow us to detect skin cancer in the superficial layer of skin, before its penetration into the dermis.

WILCPR is a wavelength independent tunable liquid crystal polarization rotator that we developed to operate with tunable

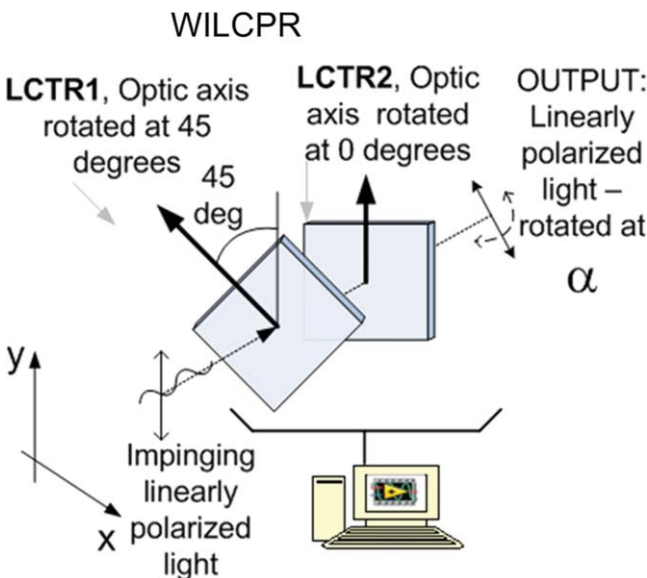


**Fig. 6** Schematic of the WILCPR, linearly polarized light impinges from the left side into the first retarder LCTR1 (oriented at 45 deg), then through the second retarder LCTR2 (oriented at 0 deg), tuned to behave as a tunable QWP. Rotation control for the output is executed by the voltage control of LCTR1 for any wavelength selected by the LCTF.

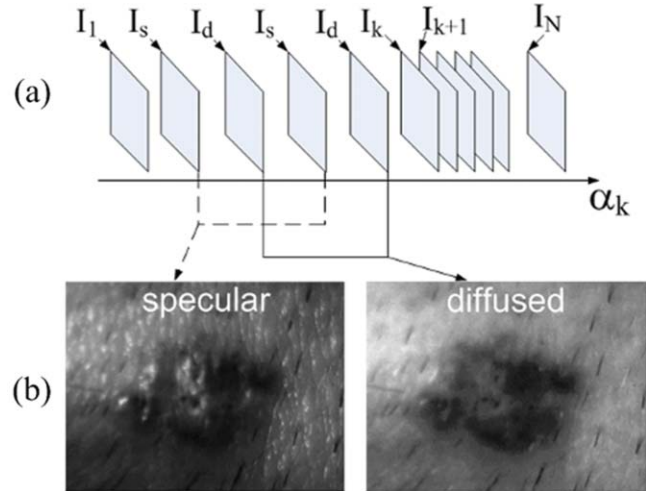


**Fig. 7** (a)  $N$  frames are taken during continuous change in  $\alpha_k$ , the rotation angle of the impinging light on the tissue.  $I_s$  is the image where a prominent specular-like light appears.  $I_d$  is obtained when most of the light is backscattered from internal layers of the tissue and no specular-like light is observed. (b) An example of BCC lesion for  $I_s$  and  $I_d$  situations.

filters such as LEO. Two nematic LC retarders comprise the device; see Fig. 6, LC tunable retarder1—LCTR1 and LCTR2. Linearly polarized light impinges from the left side into the first retarder LCTR1 (oriented at 45 deg), then through the second retarder LCTR2 (oriented at 0 deg) that is tuned by voltage  $V_5$  to behave as a tunable quarter wave-plate (QWP). Rotation control for output is executed by voltage control  $V_4$  on LCTR1 and synchronized with the algorithm of CCD camera during image capture.

WILCPR is able to rotate, continuously, a linearly polarized light for a spectral range of 450 to 1000 nm while keeping it linear. Jones matrix for a stack of the two retarders is given by Eq. (3). We omitted the accumulated total phase term from the ordinary and extraordinary modes.  $\delta_4$  and  $\delta_5$  are retardations calculated by integration over LC thickness  $d_4$  and  $d_5$ , Eq. (2). QWP condition is achieved for each wavelength by tuning voltage  $V_5$  so that  $\delta_5$  at each wavelength is tuned to be  $\pi/2$ . Jones matrix for such a system is:

$$W = \begin{bmatrix} -j \cos(\delta_4/2) - \sin(\delta_4/2) \\ -j \sin(\delta_4/2) \cos(\delta_4/2) \end{bmatrix}. \quad (3)$$

For incident linear polarization along the  $x$  axis, Jones vector is  $J_{in} = (1 \ 0)^T$  and hence the output Jones vector will be:

$$J_{out} = W \cdot J_{in} = -j \begin{bmatrix} \cos(\delta_4/2) \\ \sin(\delta_4/2) \end{bmatrix}. \quad (4)$$

From Eq. (4), the output polarization is linear and oriented at an angle equal to  $\delta_4/2$  which is governed by voltage  $V_4$ . The device is able to rotate the polarization by any degree, for a spectral range from 400 nm to more than 1000 nm in about 50 ms switching time, and between adjacent discrete angles the device is even faster. Due to that, it is possible to synchronize the capture by the CCD camera to the rotation of the impinging polarized light.

### 2.3 Scanning Method and Post Processing

Boundaries and high scattering zones are more sensitive to changes of the incident light polarization angle  $\alpha_k$ . Thus, rapid changes will be generated in the images between two or more angles  $\alpha_k$ , namely adjacent angles, say  $\alpha_{k+2}, \alpha_{k+1}, \alpha_k$  as shown in Fig. 7, when  $I_k$  is the image intensity. On the contrary, areas that already experienced denaturation of the dermis or epidermis layers will exhibit weak differences between images at different angles of the impinging polarization. While rotating the incident polarization, DOSI produces the sequence of images  $I_k$ , as shown in Fig. 7,  $k = 1$  to  $N$ .  $N$  is the number of the total frames and  $k$  is the number of the  $k$ th frame in the sequence. Sequence is captured while the WILCPR rotates the polarization ( $\alpha_k$ ). The reason for that is to improve the signal-to-noise ratio, particularly important for regions with small contrast. Equation (5) demonstrates calculated contrast between two adjacent angles. High scattering areas in  $C_{\lambda,k}$  will be averaged in the final post-processed image of  $C_{\lambda,A}$  defined in Eq. (6). This can be done online during the scan or right after the capture process is over.

$$C_{\lambda,k} = \frac{|I_{\lambda,k+2} - I_{\lambda,k}|}{I_{\lambda,k+2} + I_{\lambda,k}}, \quad (5)$$

$$C_{\lambda,A} = \frac{1}{N-2} \sum_{k=1}^{N-2} C_{\lambda,k}. \quad (6)$$

Among the whole sequence of images, a specular-like reflection can be seen clearly from the superficial stratum. These images were marked as  $I_s$  in Fig. 7(a), where  $s$  stands for pictures with specular-like signatures usually happen when incident polarization is “parallel” to the analyzer. Between the  $I_s$  (picture grabbed when  $\alpha_k = 0$ ) images, there are diffusive images  $I_d$  (picture grabbed when  $\alpha_k = 90$ ). To demonstrate this we show in Fig. 7(b) two examples of  $I_s$  and  $I_d$  of basal cell carcinoma (BCC) obtained at polarization (C in Fig. 1) angles 0 and 90 deg with respect to the fixed entrance polarizer (E in Fig. 1). In a similar manner to the definition of the second Stokes parameter<sup>31</sup> we define the following SD image in Eq. (7), designating the difference image between the specular-like (S) and diffusive (D) images:

$$SD = (I_s - I_d)/(I_s + I_d). \quad (7)$$

This represents the image generated by the photons that underwent different depolarization due to different polarization of the incident light. To explain this, first consider the incident  $p$ -polarized light, at which case the specular light is not blocked by the analyzer ( $p$ -polarization). We call this intensity  $I_p$ . Deeply depolarized light loses its DOP due to many scatterings (DOP = 0). Let us call it  $B_p$ . Due to the analyzer, only half of it will pass to the CCD. In addition, there is also a small portion of polarized light mainly from the first thin layer of the lesion. Let us call them  $P_p$  and  $S_p$ . When  $P_p$  is  $P$ -polarized light, it stems from incident light with  $p$ -polarization, and  $S_p$  is  $S$ -polarized light, stems from incident light with  $p$ -polarization. Since the analyzer is  $p$ -polarizer the  $S_p$  will not pass to the CCD. Thus, we get  $I_s$  as in Eq. (8).

$$I_s = I_p + \frac{B_p}{2} + P_p. \quad (8)$$

A similar analytical process can be formulated for  $I_d$ , when the incident light has  $S$ -polarization (electric field perpendicular

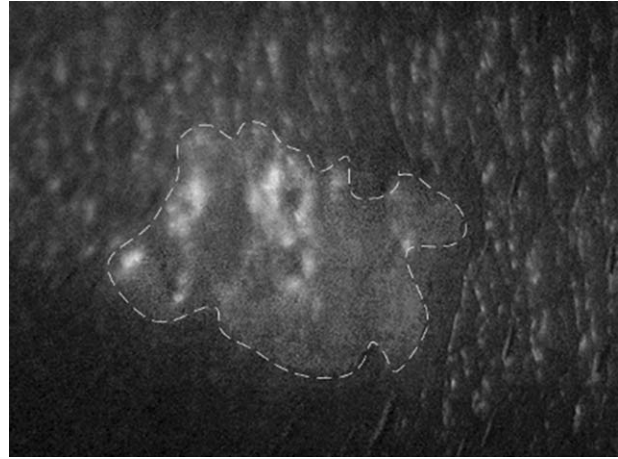


**Fig. 8** SD image for the contrast between the two images in Fig. 7(b) illustrating an emergence of well-defined boundaries of the BCC.

to the page). The specular light is blocked by the analyzer so it has no representation in  $I_d$ . Background depolarized light,  $B_s$ , now is different from  $B_p$  due to a different polarization angle of the incident light. In addition, there is a small portion of the scattered light,  $S_s$  and  $P_s$ , that still has DOP. When  $P_s$  is  $P$ -polarized light, it stems from incident light with  $s$ -polarization, and  $S_s$  is  $S$ -polarized light, that stems from incident light with  $s$ -polarization.  $S_s$  will not pass to the CCD due to the analyzer which is fixed at  $p$ -polarization. Thus,  $I_d$  can be formulated as in Eq. (9)

$$I_d = \frac{BS}{2} + P_s. \quad (9)$$

Returning to Eq. (7), SD will take the form of:

$$SD = \frac{I_p + (P_p - P_s) + \left(\frac{B_p - B_s}{2}\right)}{I_p + (P_p + P_s) + \frac{B_p + B_s}{2}}. \quad (10)$$

From Eq. (10) it is clear that the contrast originates mainly in  $B_p$  and  $B_s$ , because the background of BP and BS will always be different.  $P_p$  and  $P_s$  also increase the contrast since the light that keeps some DOP will also be different depending on the polarization of the incident light. Hence, SD helps to emphasize the lesion area and lesion boundaries by two mechanisms—polarization change in the first layer ( $P_p - P_s$ ) and different attenuations ( $B_p - B_s$ ), scattering and absorption of the backscattered light originates in deeper layers. Note, that the SD image resembles the normalized Stokes image  $S_1/S_0$ . Nevertheless,  $I_s$  and  $I_d$  are not orthogonal in the mathematical sense because the analyzer is fixed and subtraction  $I_s - I_d$  is performed at different backscattered backgrounds  $B_p$  and  $B_s$  as explained before.

Figure 8 shows an example of the SD image which shows features not seen in  $I_s$  and  $I_d$ . Well-defined boundaries are important information before executing the MMS. The SD parameter gives additional information to compare with our main approach [Eqs. (6) and (11)].

We are interested in frames excluding those with the specular-like reflection, so that the polarization changes of the backscattered light from underneath the stratum corneum can be collected and emphasized.  $C_{\lambda,k}$  in Eq. (5) is the basic differential contrast and  $C_{\lambda,A}$  in Eq. (6) is a result of collecting

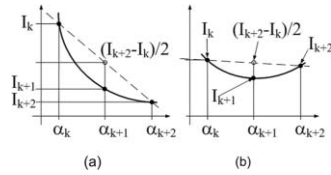


**Fig. 9** (a) The variation of the intensity in an arbitrary pixel at the CCD camera while  $\alpha_k$  changes. The solid line represents fitted continuous intensity variation while the black circles are its numerical samples. (b) Demonstration of a case where practically there is no change between  $I_k$  and  $I_{k+2}$  but the image  $I_{k+1}$  exhibits some noise and should not be taken in account in Eq. (11).

and averaging a range of pictures at different  $\alpha_k$  angles. In addition, we define an image that represents the curvature  $D_\lambda$  of the intensity on the CCD readout during changes in  $\alpha_k$  of the incident polarization. Let us take three points of intensity (arbitrary pixel)  $I_k$ ,  $I_{k+1}$ , and  $I_{k+2}$ . The numerical second order derivation, as can be found in any mathematical handbooks, is:  $\Delta^2 I / \Delta \alpha^2 = [(I_{k+2} + I_k) / 2 - I_{k+1}] / \Delta \alpha^2$ .  $\Delta \alpha^2 = (\alpha_{k+1} - \alpha_k)^2$  is the numerical constant. Let us follow the sampled signal on one of the CCD pixels as shown in Figs. 9(a) and 9(b), where the axes are the intensity on a particular pixel versus discrete polarization angle,  $\alpha_k$ , of the incident light. To express the image  $D_\lambda$  we use the magnitude of the distance between the sampled intensity at point  $(\alpha_{k+1}, I_{k+1})$ , and the average value between two adjacent points  $(I_{k+2} + I_k) / 2$ .

To avoid the cases when the change between two points  $I_{k+2}$  and  $I_k$  is not prominent or originating from noise, we multiply by the difference  $|I_{k+2} - I_k|$ . During the scan the angle of impinged polarization on a lesion changes continuously. Hence, we expect a continuous change on the CCD as well, so if the image  $I_{k+2}$  does not change much compared to  $I_k$ , we interpret the jump in  $I_{k+1}$  as a noise which can be ignored. This is demonstrated in Fig. 9(b), taking into account multiplication by  $|I_{k+2} - I_k|$  in

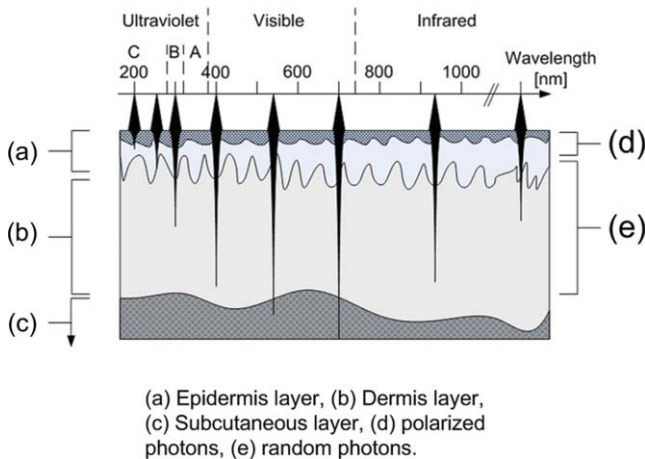


**Fig. 10** Schematic description of penetration of light through tissue. For deep penetration, such as in area (e), the backscattered light will produce a background reflection almost constant with the rotating linear polarization due to strong depolarization. (a) Stratum corneum and epidermis layers, (b) dermis layer, (c) subcutaneous layer. In regions (d) and (e), polarized photons and random photons are obtained, respectively.

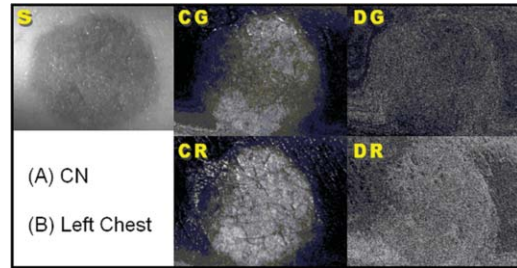


**Fig. 11** Lesion type CN, localized at the left chest.

Eq. (11).

$$D_\lambda = \frac{1}{\Delta \alpha^2 (N-1)} \sum_{k=1}^{N-2} |I_{\lambda,k+2} - I_{\lambda,k}| \times \left| \frac{I_{\lambda,k+2} + I_{\lambda,k}}{2} - I_{\lambda,k+1} \right|$$

$\lambda = 520 \text{ nm}, 700 \text{ nm}.$

(11)

In other words, Eq. (11) collects cases similar to Fig. 9(a) when there is a prominent difference between  $I_k$ , and  $I_{k+2}$  [in a similar manner to Eq. (5) which is enforced with the magnitude of the intensity difference between points  $I_k$ , and  $I_{k+2}$ ]. The differential polarization scanning method of DOSI is considering the fact that deep layers will cause the impinged polarized light to loose its polarization and emerge as a nonpolarized background light. So Eqs. (6) and (1) will mainly emphasize the changes of the superficial layer of the lesion, while still some DOP is preserved.

In Fig. 10 we illustrate qualitatively the penetration depth and marked the area where the changes in the impinged polarization can be manifested in differential changes in the polarization of the backscattered light [Fig. 10(d)]. On the contrary to deep penetration [Fig. 10(e)], the backscattered light will produce a background reflection almost constant while rotating the linearly polarized impinged light (nearly completely depolarized light). So the main information produced by Eqs. (6) and (11) in the post-processing will be due to scattered light in-between the stratum corneum and the subcutaneous layer or dermis layer. Post-processing of the DOSI system will present images  $C_{\lambda,A}$  versus  $D_\lambda$  as images with gray scale colormap. The code is

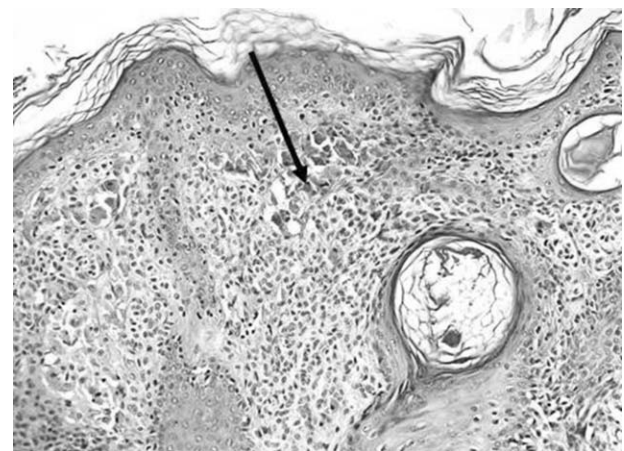


**Fig. 12** The lesion shows some features of melanocytic cytologic atypia (enlarged cells with increased nuclear size variation and enlarged nucleoli).

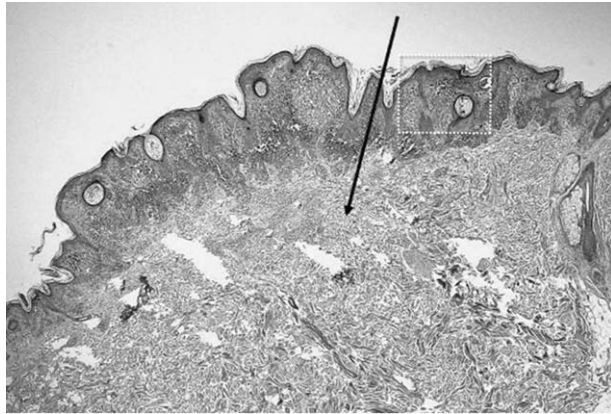


**Fig. 13** Algorithm D shows homogeneous distribution of the benign lesion probably due to a relatively ordered collagen. The white vacuaries are tears in the tissue when the lesion was cut from its wax holder cube.

written using MATLAB with the flexibility to emphasize layers of the output images. This virtue is useful to detect patterns among noisy images, and will be used in Sec. 3.

The number of patients that participated in this study was 44, ages 18 to 101, who were scheduled for removal of 77 skin lesions. *In vivo* images were obtained in the Department of Plastic and Reconstructive Surgery and Burn Unit at Soroka University Hospital. Images of skin tumors were captured before the patients entered into the operation room for their surgery. The ABCD method was used by the dermatologist and the MMS surgeon in the clinic before the patient had the surgery. We used their diagnosis in the clinic and compared it with the histology findings and attached it to DOSI images for categorization. Images were sorted into different types of skin lesions: 10-Seborheic Keratoses (SK), 13-Compound nevus (CN), 6-Junctional nevus (JN), 11-Intradermal nevus (IDN), 5-Basal cell carcinoma (BCC), 2-Pigmented basal cell carcinoma (PIG BCC), 4-Squamous cell carcinoma (SCC), 1-Hemangioma, 4-Lentigo, 16-Dysplastic nevus, and 5-Melanoma. We looked for repeating features of images for each tumor (which was histologically diagnosed) and built a database.

### 3 Measurements and Results

Among many lesions scanned we choose to present in this article a set of examples that represent the sorting of post-processed pat-

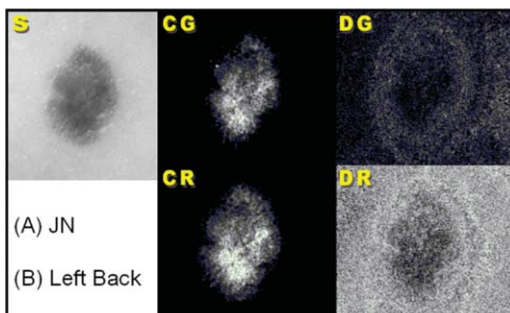


**Fig. 14** Lesion type, JN, localized at the left back.

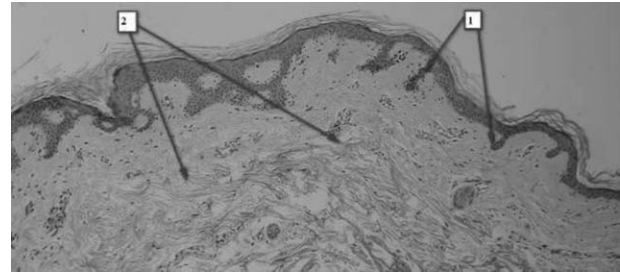


**Fig. 15** (1) Irregularly distributed and elongated epithelial buds producing a dusty irregular margin. (2) Histological picture showing a regular characteristic of the collagen, which may be the reason why in algorithm D in Fig. 14, no prominent boundaries were seen.

terns starting with what appeared to be benign lesions and ending with dysplasia, which might degrade into neoplasm such as in the case of CMM. Skin cancers like BCC and SCC are highly recognizable due to their crispy look of the stratum corneum. Our interest is in the so-called “innocent” lesions that look like an ordinary mole (starting atypical) usually ignored by most people without receiving any dermatologic inspection in the clinic. We analyze the DOSI post-process using Eqs. (6) and Eq. (11) which are presented here in four pictures marked as CG, DG and CR, DR, see Fig. 11 for an example, where C and D correspond to the images obtained using algorithms of the average of contrasts between frames [Eq. (6)] and degree of curvature [Eq. (11)] correspondingly, G and R correspond to the two wavelengths 520 and 700 nm (different penetration depths, see Fig. 10) in which imaging was performed. *S* indicates source or intensity of lesion’s picture using simple digital camera as a reference. Under each *S*-picture the reader can find physical details about the lesion, (A) histological diagnosis, (B) where the lesion was localized in the patients body. For few images it was clear that they have some degree of correlation between C and D, simply by observation. It will be shown that high correlation between C and D images can be related to dysplasia. For the sake of our argument we named this parameter as CORV (correlation by vision) pointing to the correlation between the patterns inside C images versus patterns inside D images. High-CORV is obtained when the patterns in the C- and D- images (CG versus DG and CR versus DR) are highly similar to each other and low-CORV is when the images of C and D do not look similar. The latter occurs mainly when the D-image becomes hazy and smeared compared to the C-image, which mostly emphasizes boundaries of the inner areas of a lesion when D represents the curvature of C. In Secs. 3.1 and 3.2 we illustrate the connection

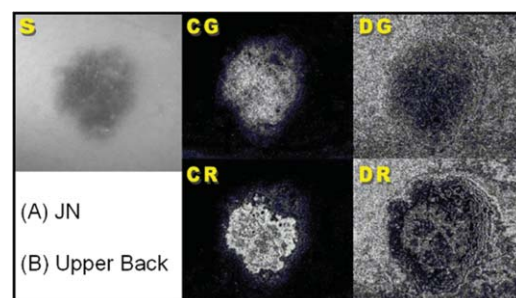


**Fig. 16** Lesion type, JN, localized at the upper back.

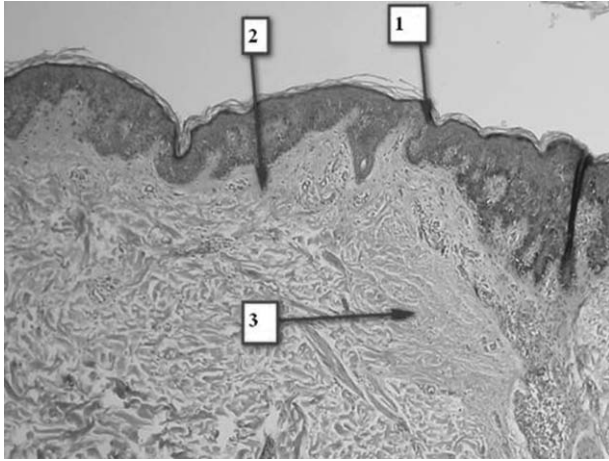


**Fig. 17** (1) Superficial melanocytes located in the junctional region of epidermis might cause G-images to be smeared or hazy. Another reason for this hazy look is that (2) the density of the collagen is equally distributed within the lesion. (3) Strong density of collagen as bundles in the deeper layers where its distribution is versatile in different areas of the lesion. Thus, DR shows distinguished patterns due to better penetration at wavelength of 700 nm.

between CG, DG, CR, and DR images (DOSI images) with the histological pictures. Then an enclosure will summarize DOSI concept and give new conjectures for new research directions.

### 3.1 Benign Lesion as Appearing in DOSI Images

With the assistance of the pathologists from the Soroka University Hospital, we could interpret the DOSI images according to the histological findings. The histological pictures were shown after figures S, C, and D, as in Fig. 12. Note: As mentioned before, the FOV of the camera is 8 mm, hence the diagonal of pictures S, C, and D is 8 mm. Histological pictures were grabbed by a digital camera of 10 megapixels. Arrows within the histological pictures are pointing to explanatory areas, teaching us about feasible projection between microscopic and macroscopic images. Figure 11 shows a benign lesion of CN-type. DOSI could produce a different texture especially in CG and CR images, emphasizing the boundaries of high scattering areas, when DG and DR do not show any prominent patterns. The lack of strong inner patterns might allude about the degree of dysplasia, which

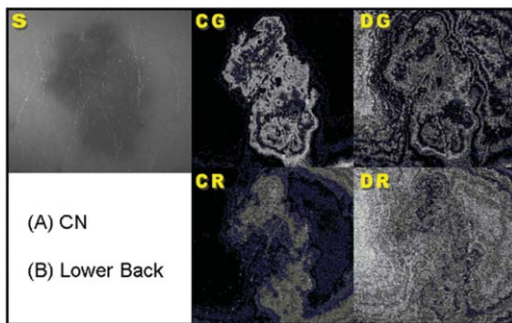


**Fig. 18** Lesion type-CN, localized at the lower back. After histological inspection it was found to have dysplastic characteristics, CN(DN). The high CORV shows similarity between algorithms C and D, thus supporting the idea of existence of dysplasm.

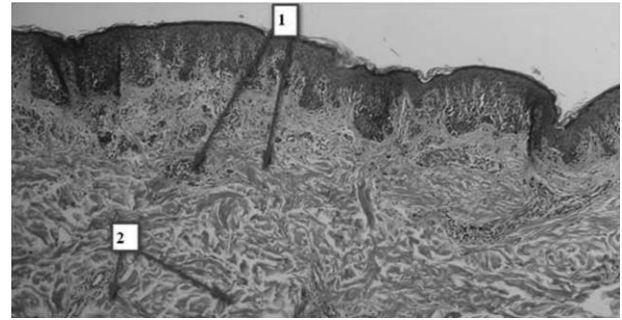


**Fig. 19** (1) Histological picture showing the intradermal component of a lesion which is located deep in the epidermis, thus C images show boundaries inside a lesion, probably representing the subepithelial collagen. (2) The degree of collagen distortion is above normal, this may lead to some patterns in the DG image in Fig. 18. This pattern is close to the dermis due to the green light used for G images.

in this case is very weak. In Fig. 12 (magnification of the dotted square in Fig. 13), a histological picture shows some features of melanocytic cytologic atypia, **enlarged cells with increased nuclear size variation and enlarged nucleoli**, which may produce this type of high scattering areas when equally distributed. In a wider view, as Fig. 13 shows, **one can see a homogeneous distribution of a benign lesion probably due to ordered collagen fiber structures**. One of the origins of the disordered collagen stems from new collagen formation of malignant lesions. In this case, neat order indicates benign lesion.

We found that as long as dysplasia was low, the CORV also was low, a fact observed in many types of the investigated lesions. For example, Figs. 14 and 15 is a case of JN, where CG and CR are showing texture of scattering areas in patterns slightly different from what is seen in the S-picture, probably due to irregularly distributed and **elongated epithelial buds producing a “dusty” irregular margin** as shown in Fig. 15(1), when algorithm D shows no prominent inner pattern because of a regular characteristic of collagen, see Fig. 15(2).

There were cases when a lesion was starting to show some degree of correlation between images of C and D Medium-CORV (Med-CORV). In these cases it is suspected that dysplasia starts to emerge as shown in CR-DR in Fig. 16 where a superficial scan (G-images) presents a hazy image, but the deeper scan (R-images) shows a pattern with a Med-CORV between CR and DR indicating upon moderate dysplasia. We suspect that dysplasia already took place over the first layer of the lesion and started

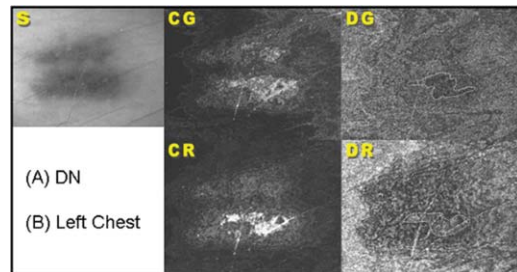


**Fig. 20** DN lesion, localized on the chest. The dashed lines in D-images are marking the similar patterns resembling patterns in C-images that reveal some CORV.

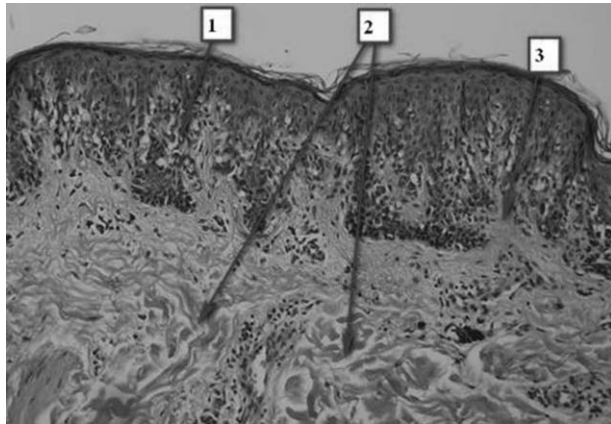


**Fig. 21** Histological picture showing weak dysplasia. (1) A low degree of dysplasia in the upper part, (2) preserved structure of dermal (deep) collagen, and (3) slightly increased density of collagen in superficial (papillary) dermis.

to penetrate the deeper layers. Sometimes when the dysplasm is strong and old it covers the upper surface first and then penetrates. That is why the G images look hazy and the R images show some patterns. Longer wavelengths like in R images target the deeper layers when the thin first layer can be almost transparent, mainly if the dysplasia finished to form patterns in the first layer and already covers equally the first layer of the lesion. This correlates to a histological picture (Fig. 17), where the collagen is bundled within the lesion and there are gaps between the bundles, that is why R-images show strong scattering with defined boundaries, when superficial melanocytes are located in the junctional region of the epidermis, and the collagen is distributed equally upon the upper part of the lesion. Thus, a smeared pattern is seen in the G-images.

A strong density of collagen can be realized also in the deeper layers as a bundled collagen increasing the scattering for longer wavelength such as in the R-images. DR shows patterns that lead us to the idea of JN with some inclination to be also dysplastic. Since dysplasia can lead to neoplasia we should be alerted when this type of sign emerges in DOSI images.

The next lesions (Figs. 18 and 19) were diagnosed in the clinic as a CN-type lesion. The DOSI scan showed clear CORV, raising our suspicion that this lesion is not a simple CN but also has dysplastic features. Indeed, after histological investigation, the lesion was found to have dysplastic characteristics, some dermatologists mark it as CN(DN). Again, dysplasm, can lead to malignancy, so following the evolution of the dysplasia over

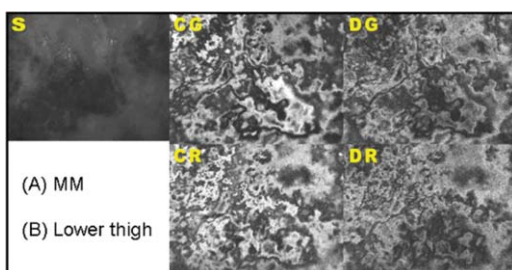


**Fig. 22** Malignant melanoma (MM) lesion, localized at the lower thigh. The lesion has very High-CORV.

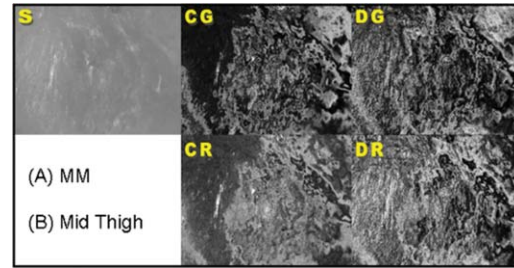


**Fig. 23** MM lesion, localized at the mid-thigh. The lesion has very high-CORV.

time with the DOSI system may be very crucial for the patients life. Histology image show mild dysplasia which manifests itself in algorithm D of Fig. 18, when CG and DG have higher CORV than CR and DR. In later examples we shall see that in malignant tissues there is very strong CORV as a strong similarity between patterns of C and D. Histology in Fig. 19 shows that collagen is denser in some areas than in normal tissue, which increases the difference in index of refraction between areas within the lesion. By contrast, in deep layers the collagen is equally distributed with intact gaps between collagen bundles, presented as a more smeared image of CR and DR with Med-CORV. Figure 18 is representing the most important goal of the DOSI method due to its ability to give some indication about the dysplastic nature of a lesion that could not be seen with a standard dermatological inspection tool (dermatoscope). When using DOSI over time, patients and physicians will have a notion about the evolution of the dysplasia and tissue distortion.

### 3.2 Dysplasia and Neoplasia as Appearing in DOSI Images

Cases of dysplasm appeared in DOSI images with good correlation between the degree of dysplasm and the degree of CORV between C and D. The higher the grade of dysplasia (or neoplasia) is, the higher the CORV. Let us review one of the scanned lesions of the DN type and its histological diagnosis that proved to be with mild dysplasia. Images in Fig. 20 enforce this idea that dysplasia can be spotted according to the degree of the CORV. C and D are showing low-CORV between patterns CG – DG and CR – DR which have a little higher CORV, see the marked areas in dashed line. In Fig. 21 we see the existence of a low degree of dysplasia in the upper part, where the deeper part preserves the natural structure of dermal collagen. Although the change in collagen density is slightly increased in the superficial (papillary)

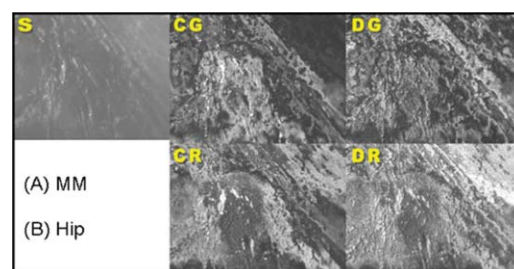


**Fig. 24** MM lesion, localized at the hip. The lesion has very high-CORV.

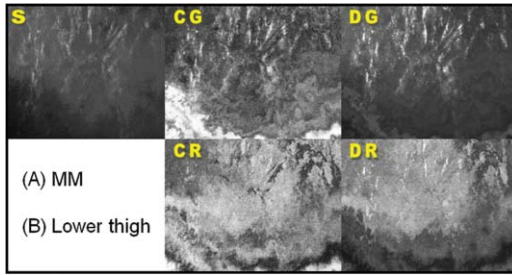


**Fig. 25** MM lesion, localized at the lower thigh. The lesion has very high-CORV.

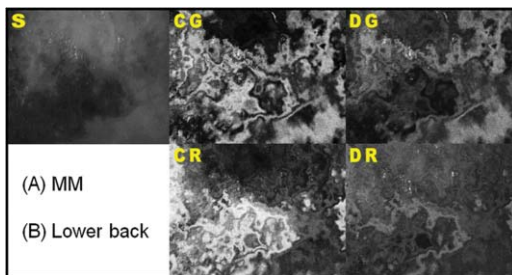


**Fig. 26** MM lesion, localized at the lower back. The lesion has very high-CORV.

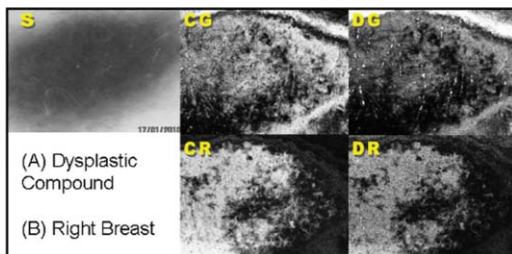


**Fig. 27** DC lesion, localized at the right breast of a female patient. In the S-picture: a clear mole can be seen with uniform gray scale. But DOSI could show distortion of tissue by CORV indicating dysplasm.

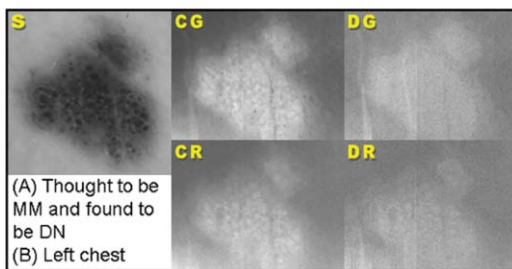


**Fig. 28** Lesion that was thought to be cancerous (CMM) while the DOSI scan showed that it is not. Histological pictures approved a low level of dysplasm but no cancer.

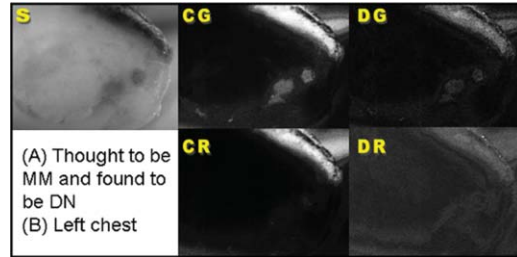


**Fig. 29** Same as Fig. 28, but a side-cut of the lesion situated in a block of wax. A brighter white can be spotted where collagen formation zone is expected.

dermis it is equally distributed, thus causing the post-processing of D-images to look a bit hazy. But it still resembles C-images, consequently have some CORV.

Progression of dysplasia to neoplasia as in the case of CMM, is a relatively slow process. In principle, we would like to be able to diagnose the premature stages of the so called innocent lesion and let the imaging system help the physician or the patient follow the lesion over time and realize whether the lesion progresses to neoplasm. We believe that pattern-sorting and the degree of the CORV are posing a feasible way to do so. To understand the worst case in which a dysplasm can be mutant to neoplasm or cancer, several cancer lesions were scanned with DOSI that are known to have a high degree of dysplasm. Strong CORV was found between C and D-images as presented in Figs. 22–26. The lesions margins in S-pictures cannot be seen because the lesion is much larger (diameter more than 1 cm) than the FOV of the CCD, which in this cases 8 mm.

This indicates a high dysplasm or distorted tissue which is expected in this type of neoplasia. These figures were chosen due to the different patterns emerging from them. Cancer cells first spread horizontally, then in later stages they start to metastasis to deeper layers toward the dermis. In this process the cell proliferation passes transient stages. One can identify patterns which are similar to those in the work of Vicsek et al.<sup>32</sup> where positional and spatial trajectories of particles were shown to be very similar to the trajectories the cancer cells plough within the healthy tissue.

Remembering the main goal to diagnose the evolving dysplasia over time, the following case of Fig. 27 is for a Caucasian woman with a seemingly innocent mole that most people would not bother themselves to check in the clinic. The DOSI scan shows very high-CORV, something that can be developed to a cancerous case. After histological inspection, the pathological diagnosis for this lesion was dysplastic compound (DC)-type nevus, with very high dysplasm. It is a classical case of using DOSI to warn the patient.

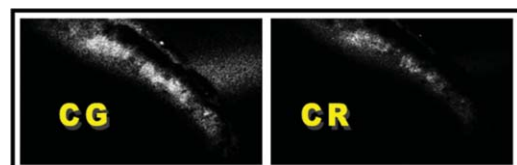


**Fig. 30** Contrast improved to emphasize the differences in the inner texture of collagen areas.

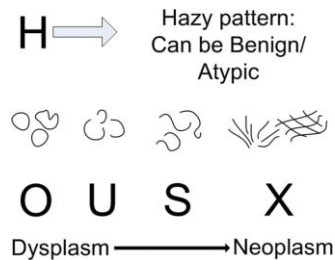


**Fig. 31** HOU SX parameter is five main patterns and their combination found by the DOSI images. H, hazy images found to be benign or just atypic with very low dysplasm, patterns from O to X are related to the degree of the dysplasia up to neoplasia where many type of patterns can be found.

In other cases similar to the lesion shown in Fig. 28, a male patient came to have his MMS after the diagnosis of three dermatologists telling him he has skin cancer. The inner area of the lesion has few degrees of colors, nonregular boundaries which can be very suspicious, etc. As can be seen in Fig. 28 there is low-CORV between C versus D-images and most important the hazy look at the D-images, which does not show circular patterns as in C images. Consequently, we suspect it is not skin cancer and maybe has some degree of low dysplasm. The patient finally had his MMS but when the histological results returned from the pathology, the histologists report was DC-type nevus, but no cancer like CMM as previously diagnosed. DOSI diagnosis was aligned with the histology.

Another area to which DOSI may contribute is to help pathologists understand, in the macroscopic point of view, the distribution of the damaged collagen and dysplasm inside the lesion. In order to have a side slice of the lesion for having its histological diagnosis, the lab technicians are using wax cubes immersion to keep the lesion after the MMS removal. This cube of wax fixes the lesion in a way so that it becomes easier for the pathologist to remove a side cut and hold it between two glasses for microscopic inspection, similar to the figures presented above. Figure 29 shows the same lesion as in Fig. 28, but now we used the DOSI scanner to reveal differences in scattering areas over the side-cut. It was very intriguing to see that DOSI can open a whole new research about the collagen quality and distribution inside a lesion only by following the scattering characteristics in the side-cut. Modifying the gray scale of the algorithm we could emphasize the small differences in texture even more Fig. 30 shows the finest contrast C-images of Fig. 29.

#### 4 Discussion and Conclusions

Changes in tissues birefringence are random and manifest in two ways, the change in the nuclear size of the melanocytes and the new generation of stiff or packed collagen, both related to dysplasm and contribute to differences in scattering. The first idea for lesion inspection was by looking for a statistical-polarimetric method using various polarization angles of the linearly polarized incident light. It is only reasonable to investigate the macroscopic changes of the lesion over time since dysplasm may get worse (evolving patterns). LCDs specifically suited for skin imaging purposes were developed and integrated into the DOSI imaging system serving the medical diagnosis purpose. These devices can be utilized for many other applications in mi-

croscopy and pathology as well. Two wavelengths were chosen, 520 and 700 nm, to cover penetrations for the epidermis and the dermis accommodating algorithms C and D. The WILCTP is composed of an LC tunable QWP and tunable retarder that change their spectral characteristics in a synchronized manner to the LCTF. More important is their ability to be synchronized with a digital camera due to the right width of the LC cells so the switching time for the LCD will be fast enough to follow the camera frame rate. With no moving parts, it is a crucial property since the DOSI algorithm is executing on each pixel. It is necessary not to have any mechanical movement during the scan to avoid smearing in DOSI algorithms, otherwise a false subtraction or addition can distort C and D images. Precise control by our LABVIEW controller enabled the demanded calibrations for the LC to make DOSI operable with MATLAB code that was built as a core of post-processing.

DOSI produces a new type of images. Using collaboration between dermatologists, surgeons, and pathologies from Soroka Hospital, differences in patterns without *a priori* knowledge were realized. For many kinds of lesions studied, the healthy condition of collagen results in similar images as can be seen by the DOSI images. On the molecular level, each type of lesion experiences a different microscopic process, but the deformation of dysplasm or simply macroscopic changes in birefringence can be sorted by DOSI in five types of major patterns, H, O, U, S, X, see Fig. 31, H stands for hazy or smeared images thus pointing to a benign lesion, O - circular patterns, U is U shape patterns, S is S shape patterns, and X is the worst case of straight line patterns which resemble the many types of plough cancerous cells living in the tissue. The conjecture is that the HOU SX\* parameter represents the cell movement or formation for four tissue conditions, benign, atypic, dysplasm, and neoplasm. The patterns resemble a characteristic of cell proliferation or cell movements as numerically explained by Vicsek et al.<sup>32</sup> (see Fig. 7) for general particle movement. In addition Brown et al.<sup>33</sup> showed numerical simulations illustrating patterns of a system undergoing spinodal decomposition (Fig. 1 in Brown et al. article)<sup>33</sup> very much like the cases of Figs. 22–26, but mainly Fig. 22. The conjecture and the investigation of the spinodal decomposition of cancer cells is far beyond the scope of this paper but, as a conjecture, the resemblance between scattering images of the DOSI system and the last two papers are prominent, however, it needs further investigation. After all, the HOU SX parameter is a model that stands for itself. Lesions may be categorized according to HOU SX and its combinations.

The second parameter for macroscopic diagnosis using DOSI algorithms is the degree of correlation by vision, CORV, as described previously. CORV was found to be degree of similarity of C-images compared with D-images, and can be a computerized process in the future. The higher the CORV, the higher the probability that dysplasia is prominent or even becomes a neoplasm, just like in the cases of CMM in Figs. 22–26 (compare with the other lesions which show a low-CORV). When using short wavelengths the patterns stem from changes of the melanocytes nuclear size and new aggregation of cells in larger clusters, which happens mainly in the superficial layers of the

\*HOU SX sounds like “house-6” after the five patterns of macroscopic diagnosis, when the 6th is their combinations, for instance in hard neoplasm a combination of OUX patterns can be found. “house” refers to the building blocks of the six sort of patterns.

epidermis. CORV is substantial when using longer wavelengths for deeper penetration where changes in collagen bundles start to deform and generate stiff and new collagen. New collagen is arranged differently than an old and healthy collagen, causing macroscopic change in a lesion as shown in Fig. 21(3). We believe that the DOSI concept should also be utilized to pathology or *in vitro* diagnosis where changes in texture of a sampled tissue are inspected. This may open a new understanding about the pathological evolution in tissues.

To summarize, a new approach was demonstrated for diagnosis of skin lesions. New images were grabbed by the DOSI system relying on three ingredients: 1. LC devices: LCTF and WILCPR which were designed especially for the DOSI system with the bearable tolerance for switching time and synchronization with a digital camera 2. Accurate calibration and control program to manage connection of LCTF, WILCPR, and digital camera. 3. Algorithms: three DOSI algorithms as the core of the approach: SD-algorithm, for lesion boundary check, C-algorithm gives the average scattering and D-algorithm which relates to the curvature of the C-algorithm with noise elimination. DOSI can perform spectrally, different wavelengths for different penetrations, when the differentiations are in various contrasts as in C and D algorithms. A DOSI system was operable in Soroka Hospital under supervision of the surgeon who was responsible for the lesion, removal. Every DOSI image was compared to its histological diagnosis with the assistance of the pathology department of the hospital. Very strong differences were realized between benign lesions, dysplastic lesions and neoplasm cases. DOSI was aimed to target macroscopic deformation of epidermis and dermis as indicators for pathological changes in the skin heading toward malignancy or neoplasia. New directions of research are proposed to computerize the imaging process as pattern recognition for CORV evaluation and macroscopic behavior of cell movement affecting deformations in new clustering of the atypic melanocytes, and in deeper layers deformation of new pathological collagen. In striving to catch innocent lesions before bursting to a cancerous case we are offering a noninvasive DOSI approach as a new way to tackle the problem.

## References

1. <http://www.cancer.org>.
2. C. A. Morton and R. M. Mackie, "Clinical accuracy of the diagnosis of cutaneous malignant melanoma," *Br. J. Dermatol.* **138**(2), 283–287 (1998).
3. A. M. P. Montgomery, R. A. Reisfeld, and D. A. Cheresch, "Integrin  $\alpha_v\beta_3$  rescues melanoma cells from apoptosis in three-dimensional dermal collagen," *Proc. Natl. Acad. Sci. U.S.A.* **91**(19), 8856–8860 (1994).
4. R. R. Anderson and J. A. Parrish, "The optics of human skin," *J. Invest. Dermatol.* **77**(1), 13–19 (1981).
5. V. Backman, R. Gurjar, K. Badizadegan, I. Itzkan, R. R. Dasari, L. T. Perelman, and M. S. Feld, "Polarized light scattering spectroscopy for quantitative measurement of epithelial cellular structures in situ," *IEEE J. Quantum Electron.* **5**(4), 1019–1026 (1999).
6. R. S. Gurjar, V. Backman, L. T. Perelman, I. Georgakoudi, K. Badizadegan, I. Itzkan, R. R. Dasari, and M. S. Feld, "Imaging human epithelial properties with polarized light-scattering spectroscopy," *Nat. Med.* **7**(11), 1245–1248 (2001).
7. S. L. Jacques, J. C. Ramella-Roman, and K. Lee, "Imaging skin pathology with polarized light," *J. Biomed. Opt.* **7**(3), 329–340 (2002).
8. R. R. Anderson, J. Hu, and J. A. Parrish, "Optical radiation transfer in the human skin and application in vivo remittance spectroscopy," in *Proc. Symp. on Bioengineering and the Skin*, Cardiff, Wales, July 19–21, 1979, MTP Press, Ltd., London (1980).
9. J. Philp, N. J. Carter, and C. P. Lenn, "Improved optical discrimination of skin with polarized light," *J. Soc. Cosmet. Chem.* **39**(2), 121–132 (1988).
10. R. R. Anderson, "Polarized light examination and photography of the skin," *Arch. Dermatol.* **127**(7), 1000–1005 (1991).
11. A. N. Yaroslavsky, V. Neel, and R. R. Anderson, "Demarcation of nonmelanoma skin cancer margins in thick excisions using multispectral polarized light imaging," *J. Invest. Dermatol.* **121**(2), 259–266 (2003).
12. B. Laude-Boulesteix, A. De Martino, B. Drévilion, and L. Schwartz, "Mueller polarimetric imaging system with liquid crystals," *Appl. Opt.* **43**(14), 2824–2832 (2004).
13. J. C. Ramella-Roman, K. Lee, S. A. Prahl, and S. L. Jacques, "Design, testing, and clinical studies of a handheld polarized light camera," *J. Biomed. Opt.* **9**(6), 1305–1310 (2004).
14. A. Weber, M. Cheney, Q. Smithwick, and A. Elsner, "Polarimetric imaging and blood vessel quantification," *Opt. Express* **12**(21), 5178–5190 (2004).
15. J. C. Ramella-Roman, D. Duncan, and T. A. Germer, "Out-of-plane polarimetric imaging of skin: surface and subsurface effects," in *Proc. SPIE*, San Jose, CA, pp. 142–153 (2005).
16. O. Aharon and I. Abdulhalim, "Liquid crystal Lyot tunable filter with extended free spectral range," *Opt. Express* **17**(14), 11426–11433 (2009).
17. O. Aharon and I. Abdulhalim, "Liquid crystal wavelength-independent continuous polarization rotator," *Opt. Eng.* **49**(3), 0340021 (2010).
18. C. Ye, "Construction of an optical rotator using quarter-wave plates and an optical retarder," *Opt. Eng.* **34**(10), 3031–3035 (1995).
19. <http://sine.ni.com/nips/cds/view/p/lang/en/nid/10703>.
20. R. Alfano, "Spectral polarizing tomographic Dermatoscope," U. S. Patent -6587711B1 (2003).
21. I. Abdulhalim, "Dispersion relations for liquid crystals using the anisotropic Lorentz model with geometrical effects," *Liq. Cryst.* **33**(9), 1027–1041 (2006).
22. O. Aharon, A. Safrani, R. Moses, and I. Abdulhalim, "Liquid crystal tunable filters and polarization controllers for biomedical optical imaging," *Proc. SPIE* **7050**, 70500P (2008).
23. I. Abdulhalim, R. Moses, and R. Sharon, "Biomedical optical applications of liquid crystal devices," *Acta Phys. Polo. A* **112**(5), 715–722 (2007).
24. B. Lyot, "Optical apparatus with wide field using interference of polarized light," *C. R. Acad. Sci.* **197**, 1593 (1933).
25. Y. Öhman, "A new monochromator," *Nature (London)* **41**, 157–291 (1938).
26. A. Yariv and P. Yeh, *Optical Waves in Crystals*, John Wiley, New York (1984).
27. A. Lien, "Extended Jones matrix representation for the twisted nematic liquid crystal display at oblique incidence," *Appl. Phys. Lett.* **57**(26), 2767–2770 (1990).
28. I. C. Khoo and S. T. Wu, *Optics and Nonlinear Optics of Liquid Crystals*, World Scientific, Singapore (1993).
29. I. Abdulhalim and D. Menashe, "Approximate analytic solutions for the director profile of homogeneously aligned nematic liquid crystals," *Liq. Cryst.* **37**(2), 233–239 (2010).
30. R. Zhang, W. Verkruyse, B. Choi, J. A. Viator, B. Jung, L. O. Svaas, G. Aguilar, and J. S. Nelson, "Determination of human skin optical properties from spectrophotometric measurements based on optimization by genetic algorithms," *J. Biomed. Opt.* **10**(2), 0240301 (2005).
31. R. A. Chipman, "Polarimetry," Chapter 22 in *Handbook of Optics*, Vol. 2, McGraw-Hill, New York (1995).
32. P. Szabó, M. Nagy, and T. Vicsek, "Transitions in a self-propelled-particles model with coupling of accelerations," *Phys. Rev. E* **79**(2), 0219081 (2009).
33. G. Brown, P. A. Rikvold, M. Sutton, and M. Grant, "Evolution of speckle during spinodal decomposition," *Phys. Rev. E* **60**(5), 515151 (1999).